Supporting Information for
Correlation of Yu-Shiba-Rusinov states and Kondo resonances in artificial spin arrays on an s-wave superconductor

Anand Kamlapure[1]*, Lasse Cornils[1], Rok Žitko[2,3], Maria Valentyuk[1,4], Roberto Mozara[1], Saurabh Pradhan[5], Jonas Fransson[5], Alexander I. Lichtenstein[1,4], Jens Wiebe[1]*, and Roland Wiesendanger[1]

[1]Department of Physics, University of Hamburg, Jungiusstrasse 11, D-20355 Hamburg, Germany

[2]Jožef Stefan Institute, Jamova 39, SI-1000 Ljubljana, Slovenia

[3]Faculty of Mathematics and Physics, University of Ljubljana, Jadranska 19, SI-1000 Ljubljana, Slovenia

[4]Department of Theoretical Physics and Applied Mathematics, Ural Federal University, 19 Mira Street, Yekaterinburg, 620002, Russia

[5]Department of Physics and Astronomy, Uppsala University, P.O. Box 516, Uppsala SE-751 21, Sweden

*Correspondence to: akamlapu@physnet.uni-hamburg.de, jwiebe@physnet.uni-hamburg.de

Supplementary text and figures

Experimental methods

All the experiments were carried out in a custom-built commercial cryostat (SPECS) at a temperature of $T = 1.2$ K in ultra-high vacuum. Details of the sample cleaning and cold Fe deposition can be found in Refs. [1,2]. To make different clusters of Fe atoms, we use vertical atom manipulation where Fe atoms were first transferred from the sample surface to the tip and then dropped back to the desired location. Details of the vertical atom manipulation and also the interstitial atom manipulation are described in Ref.[2]. The Ta(001)-O surface under study consists of a regular network of (3x3) plaquettes with square and circular shapes with a relative abundance of 4:1, respectively. In order to facilitate measurements with a superconducting tip, we first created Fe clusters of different sizes and shapes with more than one cluster of each type, followed by preparing a superconducting tip. Within error bars, each cluster of the same type showed qualitatively similar spectroscopic features which are different for other clusters of different sizes and shapes. For spectroscopy, we used a superconducting tip which was prepared by coating a Cr tip with Ta via a controlled dipping of the tip into the Ta substrate. For spectroscopy on very large clusters we used a W tip. The dI/dV spectra were measured with the standard lock-in technique with a modulation frequency of $f = 827$ Hz. A modulation voltage of $V_{mod} = 20$ µV (100 µV) was used for measurements of small bias range spectra with a superconducting (tungsten) tip, while, $V_{mod} = 2$-4 mV was used for measurements of large bias range spectra. To extract the local density of states from the measured spectra in the low-bias range as obtained with a superconducting tip, we used a standard deconvolution technique [2,3].

DFT calculations

To determine the structural arrangement of the Fe cluster with an IFA, we performed a set of DFT simulations using the VASP package [4,5]. A minimal supercell of the bcc(001) crystal was built from five layers of Ta atoms with a lattice constant of 3.30 Å. The supercell of the surface was chosen to reproduce the area of one (3 x 3) plaquette, as seen in STM images. All simulations were done using spin-polarized functionals using the generalized gradient approximation (GGA+U) for the exchange-correlation part [6,7]. The standard calculation was performed with $U = 4.3$ eV, $J = 0.9$ eV for the Fe d-states [8] and $U = 6$ eV, $J = 0.8$ eV for the O p-states. An enlarged cut-off energy was set up to 500 eV and the number of bands was increased by 50%. The structural optimization was performed until forces were less than 0.01 eV/Å on the $6 \times 6 \times 1$ k-points grid. We searched for the possible positions of IFAs in the first interspace of the TaO substrate, i.e. between the first and the second layer of the bcc(001)-arranged Ta atoms. These configurations of the surface with a single IFA were then compared by total energies and the induced type of reconstructions.
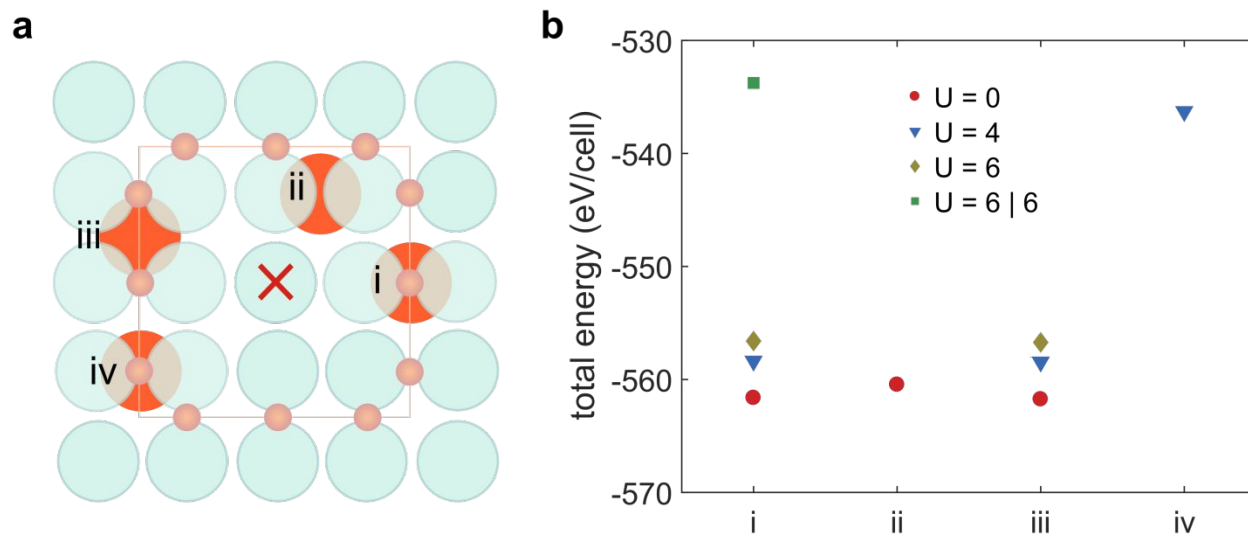
Figure S1. Interstitial Fe atom (IFA) within DFT approach. (a) Suggested positions with one IFA per (3 x 3) plaquette (initial sites) that are marked by letters (i-iv). (b) Comparison of the total energy per unit cell as obtained within GGA+U (U_{Fe-d} | U_{O-p}) simulations for different structural arrangements (i-iv).

We have also considered an additional position of an IFA in a hollow site of the Ta island. The latter configuration leads to significant reconstruction of the surface and a loss of the (3 x 3) plaquette structure, so we disregarded it. Among the other positions, one can see that, after relaxation, the IFA that was initially located on (iii) converged to location (i). In this setup, the IFA occupies approximately the center of the Ta octahedron with irregular base and two apexes, connected by the bridge oxygen atom. Among all considered configurations, only case (i) satisfies the criteria of lowest energy and smallest distortion of the surface (3 x 3) plaquette structure. To control the charge localization in the system, we used an on-site Coulomb parameter for Fe and O states, which was found to improve the convergence of the electronic and ionic minimizations significantly but did not change the structure qualitatively. The main surface change, induced by the presence of such an IFA in the first interlayer, is an elevated oxygen atom in the bridge position together with a slight upwards shift of the nearest Ta atoms. This change would be reflected in an STM image as an enhancement of the cross-like shape of the (3 x 3) plaquette near the IFA [9], which is indeed seen in the experiment (see Figure 1a of the main manuscript).

The adsorption of the Fe adatom at the center of the (3 x 3) plaquette was studied separately to account for van-der-Waals (vdW) contributions at the surface. The slab was transformed to the symmetric setup of five layers with two identical surfaces to avoid an interaction with charge images. The midpoint of the (3 x 3) plaquette coincides with the central Ta atom, which is marked as a particularly polarized atom in the surface electronic structure [9]. To account for the polarizability of the local structures on the surface, we performed a set of structural optimizations including dispersion correction energies, with an accuracy of atomic forces of less than 0.001 eV/Å. First, the slab with an adatom in the central position was relaxed using the Tkatchenko-Scheffler (TS) method [10], where all surface atoms, including the adatom, were free to relax. To account for possible corrections from the ionic states of the surface, we also included the Hirschfield iterative (HI) [11,12] partitioning scheme (TS/HI) with a self-consistent cycle [13,14]. After relaxation, the Fe adatom has a tiny in-plane offset from the symmetric central position, with a magnitude of the vector of only 0.001 Å. The extracted position of the adatom was then used to compare between different methods in simulations with both the Fe adatom and the IFA.
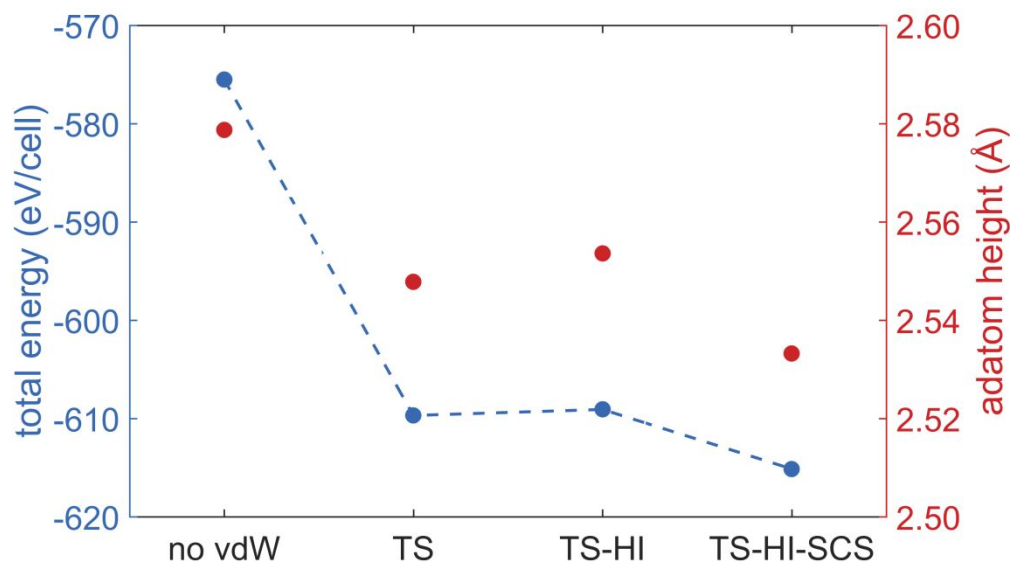
Figure S2. VdW approximations for the Fe adatom at the center of the (3 x 3) plaquette. Comparison of the heights and total energies (in the slab with two surfaces) for the system of one Fe adatom at the center of the (3 x 3) plaquette with respect to different vdW frameworks, implemented in the VASP package: no vdW (no van-der-Waals interaction), TS (Tkatchenko-Scheffler method), TS/HI (TS scheme with iterative Hirschfield partitioning) and TS/HI-SCS (self-consistent scheme of TS/HI).

The Fe adatom was allowed to move only along the *z*-direction, while the two in-plane adatom coordinates were fixed to the center position resulting from the full free relaxation of the surface within the TS/HI scheme. The reduction of the repulsive interaction between the adatom due to the dispersion forces, acting between the adatom and the polarizable substrate, is clearly visible here. This effect indicates the presence of a strong dynamical dipole-dipole interaction, that should be accounted for in the adsorption process on such surfaces, as it was predicted earlier [9]. Within a full surface relaxation, the screening TS/HI-SCS method or switching the vdW part off (no vdW) lead to the relaxation of the adatom to the nearest hollow position, which is off-center. We attribute this error to a rather effective way of the inclusion of the dynamics of the interaction between fluctuating charges as part of a pseudopotential and its possible reduction in the DFT-vdW-SCS method. The obtained height of the Fe adatom over the surface is approx. 2.5 Å (TS/HI) that fits to the experimental results [1,2].
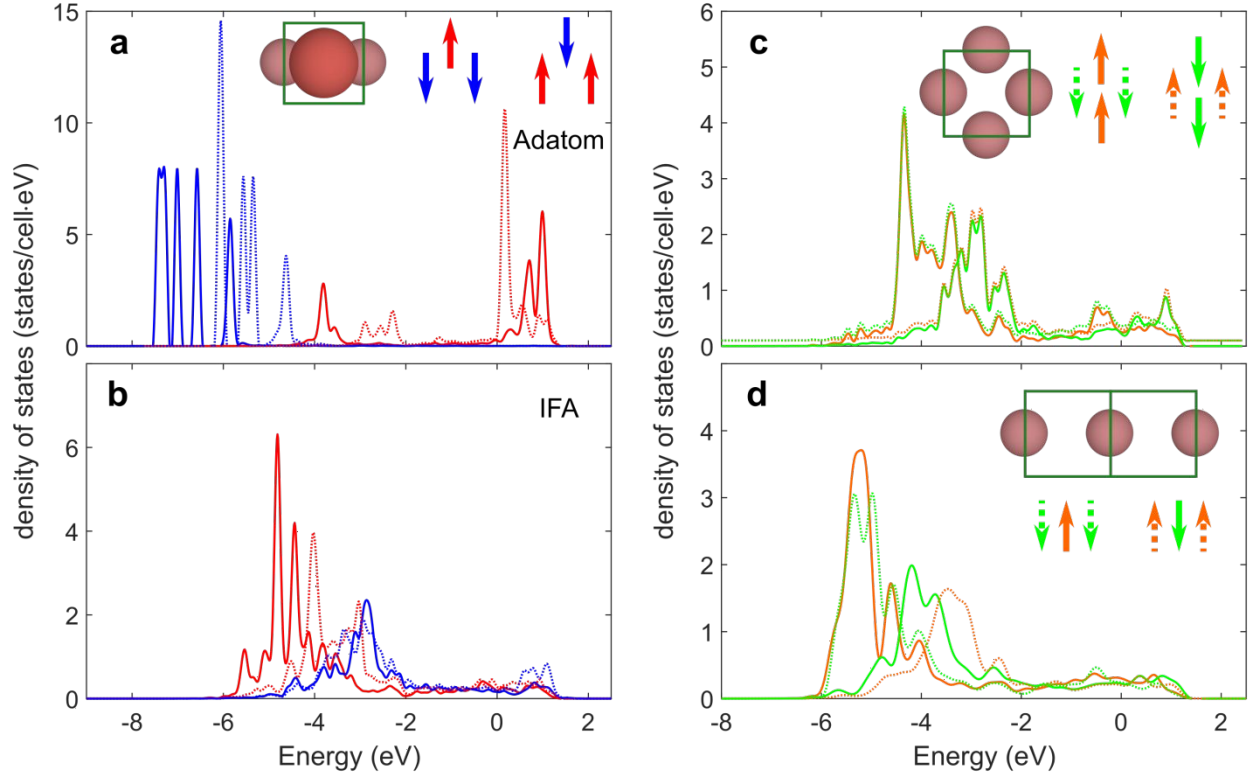
Figure S3. Magnetization of the Fe adatom in the presence of an IFA. Left: Density of states for the *d*-states of the Fe adatom (a) and the IFA (b) in the slab with both Fe atoms. Here, continuous lines refer to the slab with 2 atoms (Fe adatom and IFA) and dashed lines refer to the slab with one Fe atom in absence of the other (either adatom or IFA). Red and blue colors denote spin-up and spin-down densities, respectively. Right: Density of states for two additional IFA assemblies without Fe adatom: diamond (c) and linear (d). Here, continuous and dashed lines correspond to two sorts of IFAs in the supercell as shown in the corresponding insets. Dashed lines in (c) are shifted by 0.1 units for clarity. Due to a substantial amount of space in the bcc structure and mobility of the oxygen lattice, the IFA positions obtained from relaxation of the linear structure (d) are shifted along the z-axis with respect to each other.

The position of the adatom was extracted from the vdW calculations, while the IFA occupies the space beneath the bridge oxygen atom (case (i) in Figure S1). A few additional atomic configurations were relaxed within the spin-polarized scheme with reasonable parameters of the Coulomb interaction $U = 6.0$ eV and $J = 0.9$ eV for the d-states of Fe impurity. The other parameters were kept according to those introduced earlier as a standard calculation (see above). We observe a finite magnetic moment for both types of atoms in the main configuration (Figure S3 a,b): Fe adatom (3.1 μ_B) and IFA (1.6 μ_B). An isolated IFA has a magnetic moment of 0.9 μ_B.

Figure S3 shows the differences in the spin-polarized density of states of the Fe adatom and IFA, two additional spatial configurations of IFAs of diamond and linear form are given for comparison.

The shift of the peaks between slabs with one and two atoms in Figure S3a,b is caused by different effective U parameters used in standard and magnetic calculations for one and two atoms. Overall, one can see quite similar and small magnitudes of magnetic moments at all IFA's locations (Figure S3b,d). However, the magnetic moments get stabilized by magnetic interaction with the Fe adatom (Figure S3b). Due to the structural complexity of the host system, in particular because of the strong hybridization of the IFA to the electronic states of the substrate, we limited ourselves only to a qualitative analysis of the isotropic magnetic interactions for the selected configurations.

The IFAs are found to exhibit weak antiferromagnetic interaction among themselves, with a calculated exchange parameter[1] of J=-0.5 meV (linear, Figure S3d) and J= -4 meV (diamond, Figure S3c). In comparison, the value of the magnetic exchange interaction between the Fe adatom and an IFA is estimated to be considerably larger than between the IFAs, and has a value of J= -15.2 meV, i.e. antiferromagnetic. This result agrees very well with the experimentally extracted estimates for the exchange splitting via the exchange gap measured on the Fe adatoms.

---

[1] We used a mapping of DFT ground state energies for different spin configurations to classical isotropic Heisenberg model $H = -2\sum_{i>}^{N} J_{ij}\boldsymbol{e}_i\boldsymbol{e}_j$, where $\boldsymbol{e}_i$ - unit vector of magnetization at i-atom, N - number of magnetic atoms in the unit cell, J_{ij} - exchange interaction chosen such that $J_{AFM} < 0$. Then, for the given configurations the exchange parameter has the common form: $J = (E_{FM} - E_{AFM})/4Z$, where $E_{FM(AFM)}$ is the ground state energy of the system with FM(AFM) aligned spins, Z - number of the nearest neighbors, that have changed their direction in respect to the magnetization axis. The Heisenberg Hamiltonian can be rewritten in terms of spin operators with proper expectation values, so the J_{ij} would be also rescaled accordingly.

Fitting of the Kondo resonance

      In order to determine the Kondo temperature, we fit dI/dV spectra taken on the adatom to a Fano function given by [15]:

$$\sigma(V) \propto \sigma_0 + \sigma_1 \frac{\left(q + \dfrac{V - V_0}{\Gamma}\right)^2}{1 + \left(\dfrac{V - V_0}{\Gamma}\right)^2}$$

where q is the form factor which determines the line shape of the spectra, Γ is the half width at half maximum (HWHM), and V_0 is the bias value at the maximum of the spectra. σ_0 and σ_1 are the offset and the amplitude of the spectra, respectively.

For those spectra showing the resonance and a ZBA, we fit the dI/dV curves to the product of a Fano function and an inverted Lorentzian, given by:

$$\sigma(V) \propto \sigma_0 + \sigma_1 \left[\frac{\left(q + \dfrac{V - V_0}{\Gamma}\right)^2}{1 + \left(\dfrac{V - V_0}{\Gamma}\right)^2}\right] \times \left[1 - \frac{\sigma_2}{1 + \left(\dfrac{V - V_s}{\Gamma_s}\right)^2}\right]$$

Here, $E_s = e\Gamma_s$ is the half width in energy of the ZBA gap, V_s is the position of the gap, and σ_2 is a constant.

      Finally, we use the HWHM, Γ, to extract the Kondo temperature of each assembly and use Wilson's definition [16] to define the Kondo temperature as $T_K = 0.27e\Gamma/k_B$, where k_B is the Boltzmann constant.
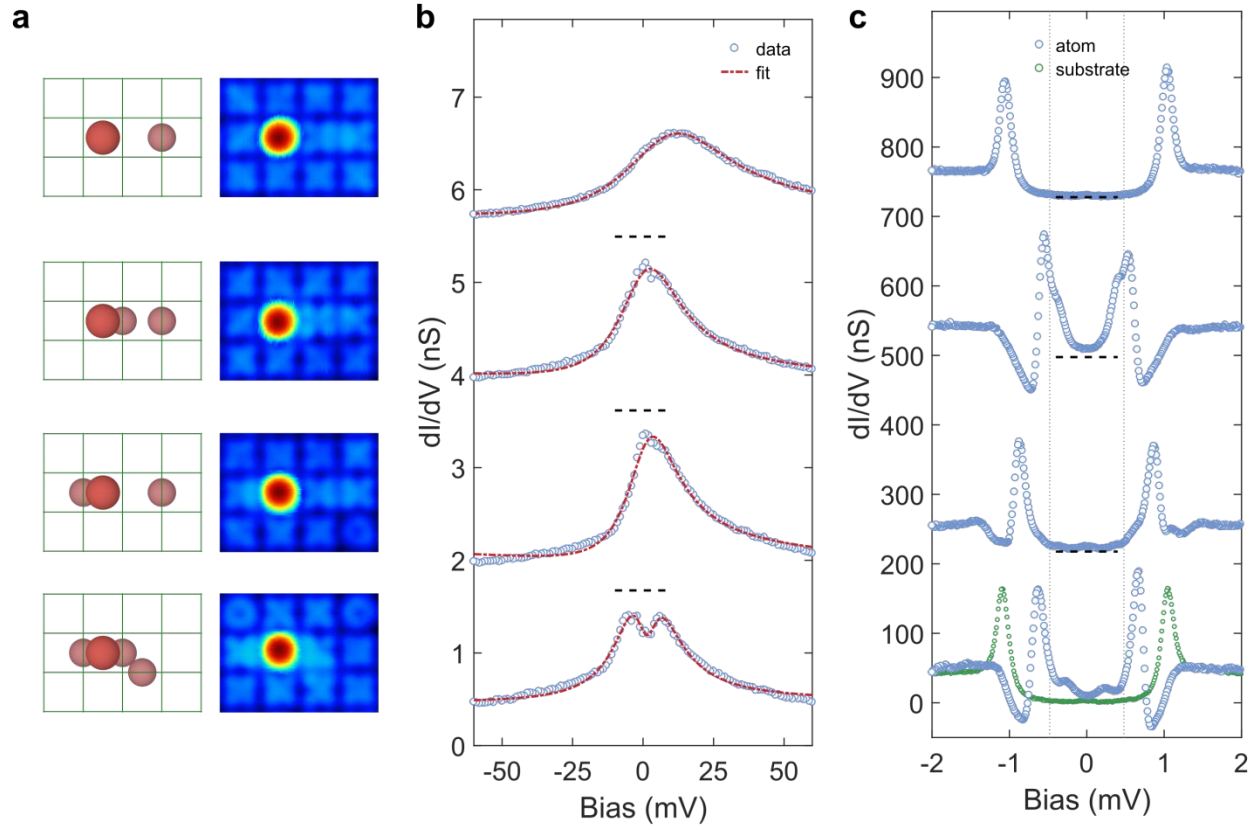
Figure S4. dI/dV spectroscopy on Fe adatoms of additional Fe clusters. (a) Schematic top view diagram and corresponding STM images of different clusters of Fe atoms. (b) Large bias range dI/dV spectra (open dots) showing the Kondo resonance. The dashed red lines are fits to a Fano function, which is multiplied by a Lorentzian dip (see above). The horizontal dashed lines are the zero lines of each spectrum, which are shifted vertically for better visibility. Stabilization parameters for STS: $V_{stab} = 100$ mV, $I_{stab} = 100$ pA, $V_{mod} = 2 - 4$ mV. (c) Small bias range dI/dV spectra measured with a superconducting tip (open dots), showing the peaks due to the YSR states. The horizontal dashed lines are the zero lines of each spectrum, which are shifted vertically for better visibility. Stabilization parameters for STS: $V_{stab} = 2.5$ mV, $I_{stab} = 100$ pA, $V_{mod} = 20$ μV.
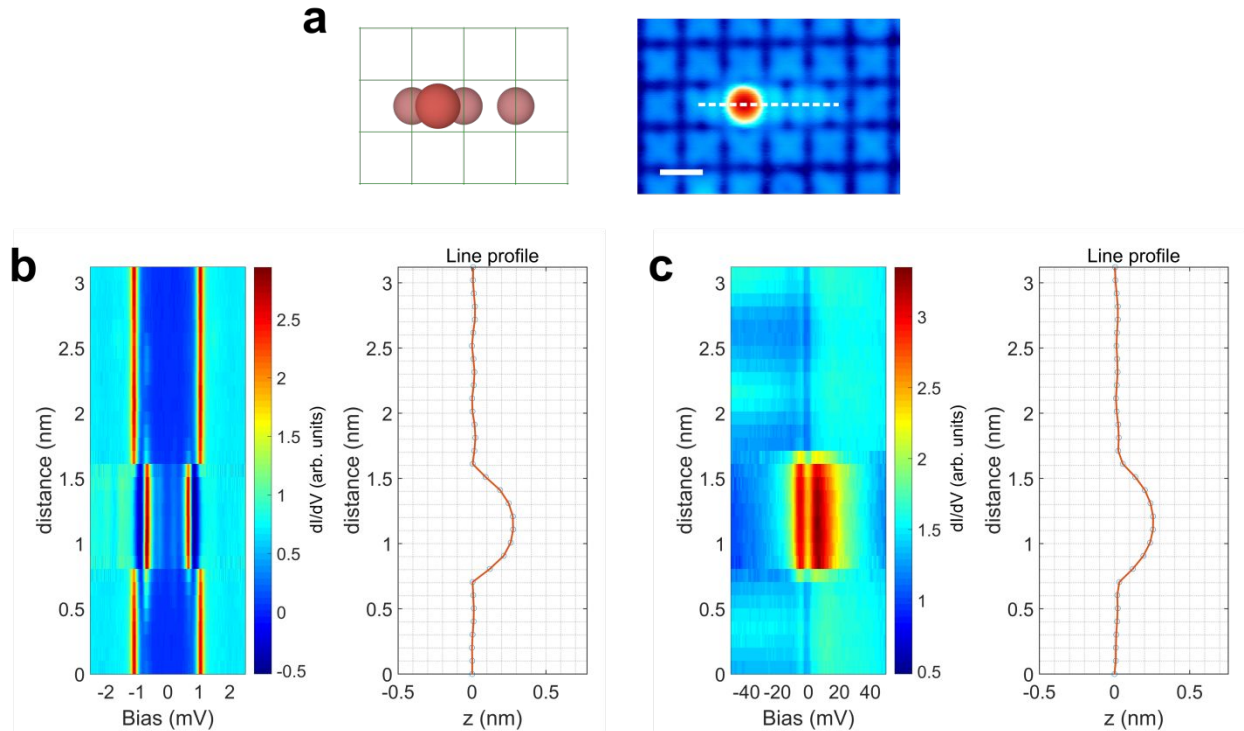
Figure S5. Spatial variation of dI/dV spectra showing YSR and Kondo features. (a) Schematic top view diagram and corresponding STM images of clusters of Fe atoms under study. The horizontal dashed white line in the STM image corresponds to the line over which spectra were measured for (b) and (c). (b-c) Left panels: 2D color map of lateral evolution of the dI/dV spectra in small (b) and large bias range (c) measured with a superconducting tip along the dashed line across the Fe cluster shown in (a). Right panels: Corresponding height of the tip z of the measurement points. From the spectral evolution, it is clear that both, the YSR peaks (b) and the Kondo resonance (c), are confined to the position of the adatom. Only a very faint intensity of the YSR state on the negative bias side is still observable at the location of the IFAs.
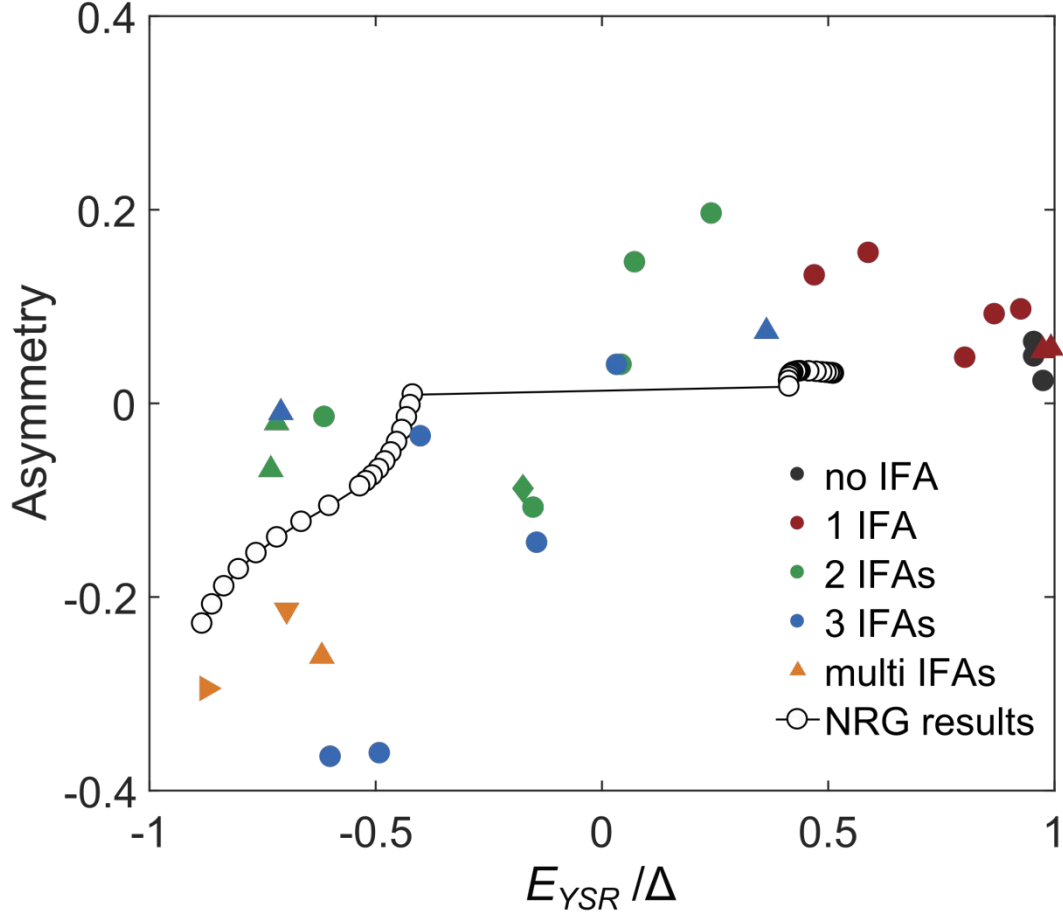
Figure S6. Asymmetry of the YSR peaks as a function of bound state energy. We observe that the intensities of the YSR peaks are asymmetric and as a general trend reverse sign with increasing number of IFAs in the assembly. To characterize this effect, we define the asymmetry as:

$$Asymmetry = \frac{h_R - h_L}{h_R + h_L},$$

where $h_R(h_L)$ is the amplitude of the YSR peak on the positive (negative) bias side. The corresponding experimental values are shown as filled symbols, where different symbols represent the various Fe clusters defined in Figure 2c of the main manuscript. The plot also shows the results of the NRG calculations for $\beta = 0$ as open dots for comparison, showing qualitative agreement with the experimental trend.

Slave-boson mean-field theory calculations

The total Hamiltonian for an Anderson impurity coupled to a superconducting substrate is $H = H_S + H_D + H_T$. Here the substrate is described by the Hamiltonian $H_S = \sum_{k\sigma} \epsilon_{k\sigma} c_{k\sigma}^\dagger c_{k\sigma} + \Delta \sum_{k\sigma} c_{k\uparrow}^\dagger c_{-k\downarrow}^\dagger$, where we assume that the substrate density of states in the normal state is constant within a bandwidth of 2D and Δ is the energy gap of the superconductor. The tunneling Hamiltonian is given by $H_T = \sum_{k\sigma} v_k \left(c_{k\sigma}^\dagger d_{i\sigma} + h.c. \right)$ and the tunneling amplitude is given by $\Gamma_i(\omega) = \pi \sum_k |v_{ik}|^2 \delta(\omega - \epsilon_k)$. Here we drop the energy dependency of the tunneling amplitude and assume that it is constant over the energy window $\Gamma_i(\omega) = \Gamma_i = 0.016D$. The Hamiltonian for the impurity is $H_D = \sum_\sigma \epsilon_d d_\sigma^\dagger d_\sigma$, where ϵ_d is the energy level of the individual impurity. We solve this model using Slave-boson mean-field theory (SBMFT) [17–22]. We restrict the Hilbert space such that there is no double occupancy in the impurity due to a large Coulomb repulsion. This is done by introducing a bosonic and fermionic degree of freedom for each electronic operator, namely $b_{i\sigma}^\dagger = f_{i\sigma}^\dagger b_i$, where $f_{i\sigma}$ is fermion and b_i is boson creation operator. No double occupancy is achieved by the constraint $b_i^\dagger b_i + \sum_{i\sigma} f_{i\sigma}^\dagger f_{i\sigma} = 1$. Within the mean-field approximation, the bosonic operator is replaced by a number and the constraint is fulfilled on an average by introducing a chemical potential.

In the large T_K limit it is favorable to break the Cooper pair such that the impurity spin can be screened. SBMFT is supposed to be valid in this regime [22,23], and thus, in particular, for our experimental setup $k_B T_K/\Delta \gg 1$. The spectrum of a single magnetic impurity in a superconductor consists of a continuum at higher energy and a bound state within the gap. This bound state appears close to the Fermi energy for small T_K and shifts towards higher energy for larger T_K. Figure 2a shows the evolution of bound states for different values of T_K.
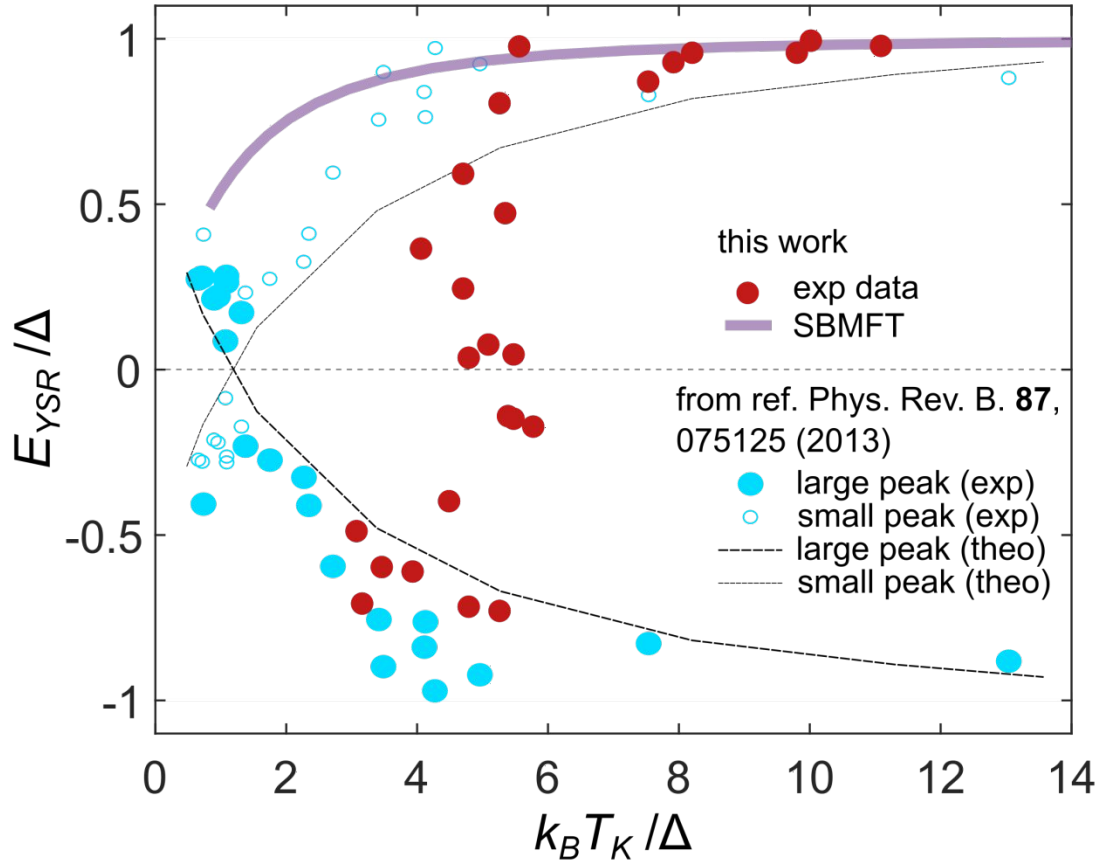
Figure S7. YSR energy versus Kondo temperature. Blue data points and black lines are adapted from the experimental data and numerical renormalization group (NRG) calculations, respectively, for the system of MnPc molecules on Pb(111) [24]. Red filled circles and the violet line represent our experimental data points and the Slave boson mean-field theory (SBMFT) calculations, respectively, for the system of Fe clusters on TaO.

Numerical renormalization group calculations

We have used the "NRG Ljubljana" implementation of the numerical renormalization group. The calculations have been performed for a two-impurity Anderson model given by:

$$H_\alpha = \sum_{k\sigma} \epsilon_k c^\dagger_{k\sigma\alpha} c_{k\sigma\alpha} - \Delta \sum_k \left(c^\dagger_{k\uparrow\alpha} c^\dagger_{-k\downarrow\alpha} + H.c. \right) + \sum_\sigma \epsilon_\alpha d^\dagger_{\sigma\alpha} d_{\sigma\alpha} + U n_{\uparrow\alpha} n_{\downarrow\alpha}$$
$$+ \sum_{k\sigma} V_{k\alpha} \left(d^\dagger_{\hat\alpha} c_{k\alpha} + H.c. \right)$$

H_{12}

$$= J\left[(1-\beta)\mathbf{s}_1 \cdot \mathbf{s}_2 + \beta s_{1,z} s_{2,z} \right] - t \sum_\sigma \left(d^\dagger_{1\sigma} d_{2\sigma} + H.c. \right) = J$$
$$\left[(1-\beta)s_{1,x} s_{2,x} + (1-\beta)s_{1,y} s_{2,y} + s_{1,z} s_{2,z} \right] - t \sum_\sigma \left(d^\dagger_{1\sigma} d_{2\sigma} + H.c. \right)$$

$H = H_1 + H_2 + H_{12}$.

Here α indexes the two impurities (α = 1, 2), σ is the spin ($\uparrow$, $\downarrow$), k is the electron momentum, ϵ_k the dispersion of band electrons, and $V_{k\alpha}$ is the hybridization between the impurity α and the superconducting band ($\Gamma = \pi\rho|V|^2$, where ρ is the density of states in the band in the absence of superconductivity). Finally, $n_{\sigma\alpha} = d^\dagger_{\sigma\alpha} d_{\sigma\alpha}$ is the occupancy operator for impurity α, while s_α is the impurity spin operator defined as $s_\alpha = (1/2) d^\dagger_{i\alpha} \boldsymbol{\sigma}_{ij} d_{j\alpha}$, where $\boldsymbol{\sigma}$ is the vector of Pauli matrices, while i,j are the internal spin indexes. The exchange interaction is a pure Heisenberg coupling for $\beta = 0$ and pure Ising coupling for $\beta = 1$. In other words, the spin-flip terms (transverse part of the exchange interaction) are progressively turned off as β evolves from 0 to 1.

We use the parameters $U_1 = U_2 = 10$, $\Gamma_1 = \Gamma_2 = 0.7$, $\epsilon_1 = -4$, $\epsilon_1 = -5$, with the gap fixed at $\Delta = 0.001$ (all parameters are expressed in units of the bandwidth). We have included a small constant hybridization between the impurities ($t = 0.02$) to suppress the sharp quantum phase transition; this is the main motivation for modelling in terms of the Anderson model instead of the pure-spin Kondo model. The overall strength of the exchange coupling is controlled by explicitly including a variable exchange coupling J. The calculations were performed for the discretization parameter $\Lambda = 2$ keeping up to 2000 state multiplets and averaging over $N_z = 4$ interleaved discretization meshes. For studying the shape of the Kondo resonance, we have

broadened the results in order to smooth out the superconducting gap. This is achieved by using the kernel that corresponds to the sine modulation used in the lock-in technique.
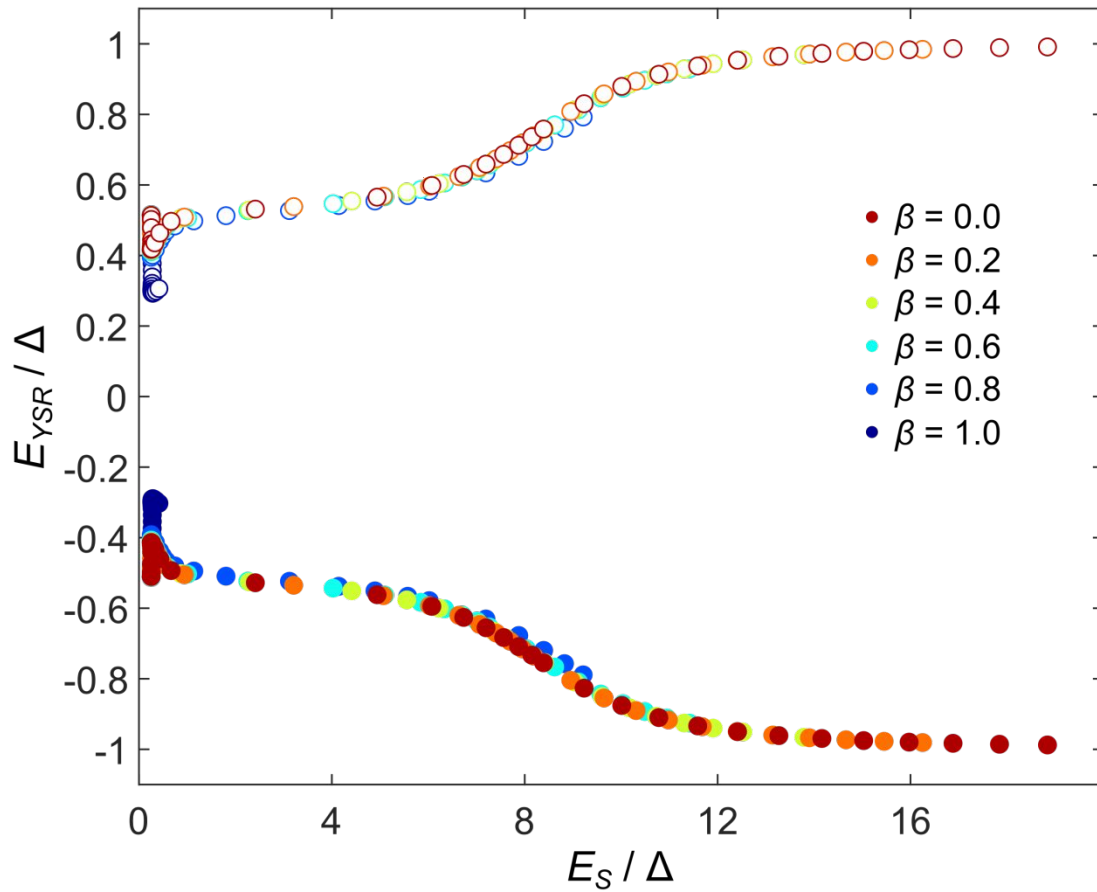
Figure S8. YSR energy versus width of the exchange splitting gap. The plot shows results of NRG calculations, where the YSR peak energy corresponding to the larger (smaller) peaks are shown as filled (empty) circles. Different colors correspond to NRG calculations for β ranging from 0 to 1.

References

1.   Cornils, L. *et al.* Spin-Resolved Spectroscopy of the Yu-Shiba-Rusinov States of Individual Atoms. *Phys. Rev. Lett.* **119**, 197002 (2017).

2.   Kamlapure, A., Cornils, L., Wiebe, J. & Wiesendanger, R. Engineering the spin couplings in atomically crafted spin chains on an elemental superconductor. *Nat. Commun.* **9**, 3253 (2018).

3.   Franke, K. J., Schulze, G. & Pascual, J. I. Competition of Superconducting Phenomena and Kondo Screening at the Nanoscale. *Science* **332**, 940–944 (2011).

4.   Kresse, G. & Furthmüller, J. Efficient iterative schemes for ab initio total-energy calculations using a plane-wave basis set. *Phys. Rev. B* **54**, 11169–11186 (1996).

5.   Blöchl, P. E. Projector augmented-wave method. *Phys. Rev. B* **50**, 17953–17979 (1994).

6.   Perdew, J. P., Burke, K. & Ernzerhof, M. Generalized Gradient Approximation Made Simple. *Phys. Rev. Lett.* **77**, 3865–3868 (1996).

7.   Dudarev, S. L., Botton, G. A., Savrasov, S. Y., Humphreys, C. J. & Sutton, A. P. Electron-energy-loss spectra and the structural stability of nickel oxide: An LSDA+U study. *Phys. Rev. B* **57**, 1505–1509 (1998).

8.   Cococcioni, M. & de Gironcoli, S. Linear response approach to the calculation of the effective interaction parameters in the LDA+U method. *Phys. Rev. B* **71**, 035105 (2005).

9.   Mozara, R. *et al.* Atomically thin oxide layer on the elemental superconductor Ta(001) surface. *Phys. Rev. Mater.* **3**, 094801 (2019).

10. Tkatchenko, A. & Scheffler, M. Accurate Molecular Van Der Waals Interactions from Ground-State Electron Density and Free-Atom Reference Data. *Phys. Rev. Lett.* **102**, 073005 (2009).

11. Bučko, T., Lebègue, S., Hafner, J. & Ángyán, J. G. Improved Density Dependent Correction for the Description of London Dispersion Forces. *J. Chem. Theory Comput.* **9**, 4293–4299 (2013).

12. Bučko, T., Lebègue, S., Ángyán, J. G. & Hafner, J. Extending the applicability of the Tkatchenko-Scheffler dispersion correction via iterative Hirshfeld partitioning. *J. Chem. Phys.* **141**, 034114 (2014).

13. Tkatchenko, A., DiStasio, R. A., Car, R. & Scheffler, M. Accurate and Efficient Method for

Many-Body van der Waals Interactions. *Phys. Rev. Lett.* **108**, 236402 (2012).

14. Bučko, T., Lebègue, S., Hafner, J. & Ángyán, J. G. Tkatchenko-Scheffler van der Waals correction method with and without self-consistent screening applied to solids. *Phys. Rev. B* **87**, 064110 (2013).

15. Fano, U. Effects of Configuration Interaction on Intensities and Phase Shifts. *Phys. Rev.* **124**, 1866–1878 (1961).

16. Khajetoorians, A. A. *et al.* Tuning emergent magnetism in a Hund's impurity. *Nat. Nanotechnol.* **10**, 958–964 (2015).

17. Coleman, P. New approach to the mixed-valence problem. *Phys. Rev. B* **29**, 3035–3044 (1984).

18. Coleman, P. Mixed valence as an almost broken symmetry. *Phys. Rev. B* **35**, 5072–5116 (1987).

19. A. Hewson. *The Kondo Problem to Heavy Fermions*. (Cambridge University Press, 1993).

20. Schwab, P. & Raimondi, R. Andreev tunneling in quantum dots: A slave-boson approach. *Phys. Rev. B* **59**, 1637–1640 (1999).

21. Aono, T., Eto, M. & Kawamura, K. Conductance through Quantum Dot Dimer Below the Kondo Temperature. *J. Phys. Soc. Japan* **67**, 1860–1863 (1998).

22. Avishai, Y., Golub, A. & Zaikin, A. D. Superconductor-quantum dot-superconductor junction in the Kondo regime. *Phys. Rev. B* **67**, 041301 (2003).

23. Borkowski, L. S. & Hirschfeld, P. J. Low-temperature properties of anisotropic superconductors with kondo impurities. *J. Low Temp. Phys.* **96**, 185–206 (1994).

24. Bauer, J., Pascual, J. I. & Franke, K. J. Microscopic resolution of the interplay of Kondo screening and superconducting pairing: Mn-phthalocyanine molecules adsorbed on superconducting Pb(111). *Phys. Rev. B* **87**, 075125 (2013).